Tracking the magmatic-hydrothermal transition in the phosphorus-rich Gatumba pegmatite dyke system (Rwanda) and its role on Sn mineralization.

Niels Hulsbosch and Philippe Muchez
KU Leuven, Department of Earth and Environmental Sciences, Division of Geology, Belgium

Abstract. Fieldwork, petrography, Raman spectroscopy and fluid inclusion microthermometry were applied to the lithium-cesium-tantalum (LCT) Gatumba pegmatite dyke system (Rwanda) to track the magmatic-hydrothermal fluid transition and its role on cassiterite mineralization. The phosphorus-rich system illustrates a magmatic-hydrothermal fluid evolution from H_2O-NaCl-KCl-(CO_2,N_2) to H_2O-NaCl-LiCl-(CO_2,N_2) fluids during solidification from the border zone inwardly to the core zone. The Gatumba dyke system is a unique case-study because the montebrasite, carbonated Mn-fluorapatite, quartz core zone is mineralized in primary cassiterite. The high Li- and P-contents in the core zone, which lowers the crystallization temperature, explains the crystallization of magmatic-hydrothermal cassiterite in this pegmatite subsystem. A late-stage H_2O-NaCl-(CO_2,N_2) fluid caused subsolidus muscovitization of the magmatic fabric and precipitation of secondary cassiterite in greisen pockets.

1 Introduction

This study evaluates the role of magmatic-hydrothermal aqueous fluids in transporting, concentrating and precipitating cassiterite during crystallization and subsolidus replacement of lithium-cesium-tantalum (LCT) family pegmatite dykes. The extreme lithiophile, rare-metal enrichment (Li, Rb, Cs, Be, Nb, Ta, Sn, etc.) in these highly peraluminous magmas has generally been interpreted as resulting from extended disequilibrium crystal fractionation of an undercooled melt. The presence, timing and petrogenetic importance of an aqueous fluid phase, coexisting with the melt, during internal textural and geochemical-mineralogical differentiation of pegmatites, is strongly debated (e.g. London 2014). However, studies indicate the potential importance of melt-fluid and melt-melt immiscibility in flux-rich pegmatite melts (Jahns and Burnham 1969; Webster et al. 1997). In addition, aqueous fluid exsolution is accepted to occur in shallow-level, miarolitic pegmatites that contain crystal-lined open cavities and show abundant fluid inclusions with the typical signature of aqueous fluids (Maneta and Anderson 2018; and references therein).

Consequently, this contribution aims to decipher the temporal and compositional evolution of magmatic-hydrothermal fluid exsolution in LCT pegmatites in order to understand the timing and role of water-saturation during pegmatite differentiation processes and late-stage crystallization at the magmatic- hydrothermal transition. The Early-Neoproterozoic LCT-family Gatumba dyke system (GDS) in Western Rwanda is selected because of its internally zoned nature with Nb-Ta-oxides and cassiterite mineralization occurring in primary magmatic and secondary metasomatic replacement units. This work will consequently (1) describe the internal anatomy of the GDS, (2) identify mineral compositional variations by Raman spectroscopy, (3) describe the microthermometric properties of magmatic, magmatic-hydrothermal and metasomatic fluid system trapped in quartz, cassiterite, and montebrasite-amblygonite crystals and (4) characterize the evolution of these fluids.

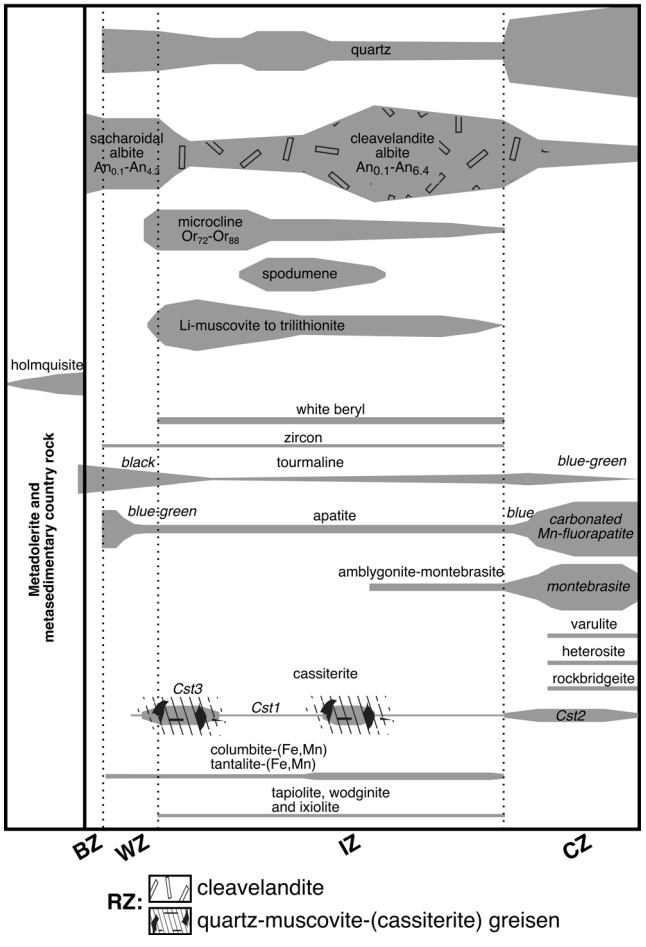

Figure 1. Internal anatomy of the Gatumba pegmatite Dyke System consisting of a border (BZ), wall (WZ), intermediate (IZ), core (CZ) and two replacement zones (RZs).

2 Results and interpretation

2.1 Internal anatomy of the GDS

Field observations in combination with a macro- and

microscopic study and Raman spectroscopic analyses of 64 hand-specimens enabled characterization of the internal anatomy of the GDS. It consists of border, wall, intermediate, quartz core and replacement zones (Fig. 1). The GDS is dominantly intruded along axial planar cleavage planes in greenschist-facies, Mesoprotozeroic metasediments (S_0 and S_1 ~260/50) and bedding-parallel metadolerite sills (S_1 ~270/30). The pegmatite bodies locally crosscut the sills. The maximum length of the GDS is ~850 m and dyke thicknesses range between ~15-40m in the metadolerites and ~3-10m in the metasediments. Small pegmatitic stringers (m- to dm-wide) occur along the cleavage planes in the metasediments.

Contact metasomatism caused locally the development of holmquistite-bearing assemblages in the metadolerites. The border zone (BZ) of the GDS developed as a sharp 0.5-1 cm thin layer and consists of hypidiomorphic and fine-grained quartz, sacharoidal albite and inwardly flaring black tourmaline crystals. The wall zone (WZ) ranges in thickness between 5 cm and 4 dm. It developed an aplitic banding (~1cm thick bands) which consists of medium-grained quartz, fine-grained albite and fine-grained, blue-green apatite. The aplite fabric (~15 cm thick) evolves dyke-inwards to a more coarse-grained (cm to dm) anisotropic fabric of inwardly elongate and flaring crystals of quartz, Li-rich micas, microcline, apatite and fine-grained albite. The latter fabric contains mm-scale tantalite-columbite crystals. The interior zone (IZ) demonstrates increased crystal sizes (m-scale) and has thicknesses varying from ~3 to ~10m. This zone is dominated by asymmetrical and dominantly discontinuous bi- to tri-mineral assemblages consisting of perthitic microcline-quartz and Li-muscovite-spodumene-quartz. Both quartz and spodumene form as dm- to m-long elongated, euhedral crystals. Primary accessory phases consist of white beryl, zircon, tourmaline, apatite, amblygonite-montebrasite, niobium-tantalum oxides and rare euhedral cassiterite. In addition, this zone is heavily affected by metasomatic replacement zones of cleavelandite after microcline (>70%) and the subsequent development of quartz-muscovite-cassiterite greisen pockets (0.5-5 dm wide). The greisen pockets can extend towards the WZ. The major part of the cassiterite occurs as subhedral and solid-inclusion-rich phases in the greisens. The core zone (CZ) can occasionally develop as a coarse monomineralic quartz unit in thinner dyke parts. However, it often formed as a cogenetic assemblage of coarse quartz, amblygonite-montebrasite and blue-apatite, together with minor fine-grained albite and euhedral cassiterite. Alteration of amblygonite-montebrasite to varulite, heterosite and rockbridgeite is observed. Based on its primary mineralogy, the GDS can be classified as an LCT-family, rare-element class, complex spodumene-subtype pegmatite.

In summary, cassiterite occurs as a primary phase in magmatic-stage microcline, and in cleavelandite units, replacing microcline, from the IZ (i.e. Cst1), but also in assemblage with primary phosphates and quartz in the CZ (i.e. Cst2). Secondary cassiterite occurs abundantly in metasomatic-replacive greisen pockets (i.e. Cst3).

2.2 Raman spectroscopy of minerals

Raman analyses were performed with a Bruker Senterra in order to determine the mineralogical variation of amblygonite-montebrasite (n=14), apatite (n=17), and cassiterite (n=29) in the GDS. The position and width of Raman bands of amblygonite-montebrasite are related to its fluorine content and enable as such characterization (Rondeau et al. 2006). Montebrasite-amblygonite in the CZ shows bands at 601.5±0.5 cm^{-1} (PO_4^{3-} bending and AlO_6^{9-} stretching vibrations), at 1058.5±0.5 cm^{-1} (PO_4^{3-} stretching vibration) and at 3369.9±0.7 cm^{-1} (OH^- stretching vibration) with a FWHM of 33.3±1.4 cm^{-1}. These observations indicate a montebrasite fluorine content of 1.8-4.5 wt.%, 0.5-4.1 wt.%, 1.4 wt.% and 2.3 wt.%, respectively, with an average of 1.8 wt.%. Based on the calibrated montebrasite F-OH exchange reaction of London et al. (2001) this relates to a low, i.e. ~0.5 wt.%, fluorine content of the melt (maximum of 1.2 wt.%).

The Raman spectra of blue apatite in the CZ show PO_4^{3-} vibrations around 965 cm^{-1} (v_1), 446 cm^{-1} (v_2), 1060 cm^{-1} (v_3) and 581 cm^{-1} (v_4); indicating fluorapatite. The spectra are, moreover, strongly complicated with the presence of sets of (very) strong vibrations at 1222 cm^{-1} (>$v_{1,PO4}$), 1322 cm^{-1}, 1422 cm^{-1} (>$v_{1,PO4}$), and a set at 1510 cm^{-1} , 1582 cm^{-1} and 1710 cm^{-1}. The presence of ~1420 cm^{-1} vibrations in fluorapatite univocally points to carbonate substitution for phosphate (i.e. $v_{3a,CO3}$ mode of $V_{3,CO3}$ doublet) and requires a paired substitution or vacancies to maintain charge balance (Tacker 2008). The paired ~1500 cm^{-1} and ~1580 cm^{-1} peaks indicate carbonate substituting for fluorine, partially charge balanced with carbonate substituting phosphate (i.e. $v_{3b,CO3}$ mode of $V_{3,CO3}$ doublet). The other peaks may arise from Davydov splitting (Tacker 2008). The shift in position of the 284 cm^{-1} (Ca-PO_4 mode), 311 cm^{-1} (Ca-F mode) and 330 cm^{-1} (Ca-OH mode) peaks towards 266 cm^{-1}, 309 cm^{-1} and 350 cm^{-1} indicates, moreover, divalent cations substituting for Ca^{2+} (cf. Penel et al. 1997). The blue color of apatite in the CZ demonstrates manganese enrichment with dominantly Mn^{2+} substituting for Ca^{2+}. The color itself originates from Mn^{5+} substituting for P^{5+} (Hughes et al. 2004).

Raman spectra of the 3 cassiterite phases (Cst1, Cst2 and Cst3) all show the characteristic A_{1G} band at 633 to 634 cm^{-1} and a less-intense, broad B_{2G} band around 730 cm^{-1} which corresponds to the symmetric and asymmetric stretching of the Sn–O bonds, respectively (Wang et al. 1993). In addition, Cst1 and Cst2 phases contain a medium-weak band at ~774 cm^{-1} in combination with a medium-intense band at ~834 cm^{-1}. Cst3 contains strong bands at ~777 cm^{-1}, ~804 cm^{-1} (i.e. infrequent), ~833 cm^{-1} and ~876 cm^{-1}. The rarely observed ~804 cm^{-1} and abundantly-observed ~830 cm^{-1} bands are assigned to broad A_n peaks caused by heterovalent substitution of W^{5+} and Nb^{5+}+Ta^{5+}, respectively (Wang et al. 1993). The ~876 cm^{-1} bands are assigned to the A_g peak of columbite-(Mn). Moreover, Cst3 shows abundant 100-450 µm large columbite-(Mn) lamellae along its growth zones. Altogether, Cst1, 2 and 3 phases demonstrate paired substitution of

$2(Nb,Ta)^{5+}+(Fe,Mn)^{2+}$ for $3Sn^{4+}$. In addition, the inclusion-rich Cst3 phase is characterized by profuse columbite-(Mn) exsolution.

2.3 Microthermometry

Detailed inclusion petrography and microthermometric measurements, with a synthetic fluid inclusion-calibrated Linkam THMS600 stage, were performed on 217 inclusions in quartz, montebrasite and cassiterite from 24 wafer sections representing all zones. Only the thin BZ and the cleavelandite RZ could not be studied for inclusions due to the fine-grained and translucent nature of the host minerals. The phase transition temperatures (T_{fm}, $T_{m,ice}$, $T_{m,hh}$, $T_{m,CO2}$, $T_{m,clath}$, $T_{h,CO2}$ and $T_{h,tot}$) were determined by slow-rate cooling to -190°C and applying a cyclic heating-cooling method both to obtain precise measurements (especially for $T_{m,ice}$ and $T_{m,hh}$) and to avoid metastability and incomplete liquid solidification effects. Important to note is that when the inclusions were only cooled to approximately -130°C, no first melting around -70°C was observed but only a sudden change in the appearance of the aqueous phase around −35°C. The latter transition could then erroneously be identified as first melting.

On the basis of petrography, six (sub-)types of fluid inclusion could be identified (L1a - L1b, L2a - L2b, and L3a - L3b) for which the main characteristics are given in Table 1. The vapor phase of CO_2-containing inclusions was analyzed with Raman spectroscopy, which detected N_2 up to 25 mol%.

Type L1 inclusions occur in quartz of WZ and IZ and are characterized by saline H_2O-NaCl-KCl-(CO_2, N_2) fluids with ~20 wt.% NaCl and ~3 wt.% KCl. Both L1a and L1b subtypes are microthermometrically similar except for (1) the presence of (Ca^{2+},Mn^{2+},Fe^{2+})-carbonates and paragonite as accidentally trapped solids in the L1a subtype, which is the predominant type in the WZ and (2) the $T_{h,tot}$ which averages 290°C for L1a and 355°C in L1b. The Na/K ratio lowers from (1) primary inclusions in growth zones in euhedral prismatic quartz to (2) (pseudo)secondary inclusions occurring as intragranular and interphase assemblages spatially related to partial microcline replacement in the cleavelandite RZ. (1). The prevalence of L1a towards the WZ, (2) lower $T_{h,tot}$ of L1a compared to L1b, (3) the presence of Mn^{2+} and Fe^{2+} carbonates as trapped solids in L1a, and (4) the presence of flaring-inwards black, $(Fe-Mg)^{2+}$ tourmaline both in the BZ and country rocks, point towards (1) the importance of conductive cooling of the hot pegmatite-forming melt at its margins by the cooler, greenschist-facies country rocks (cf. London, 2014) and, (2) the influence of small-scale mobility of mafic-elements from the country rocks to the pegmatite marginal zones.

Type L2 inclusions occur in primary assemblages in the CZ minerals and show low first melting temperatures indicating LiCl enrichment. Occasionally, L2 inclusions show accidentally trapped Li-mica crystals.

L2a subtype inclusions occur in montebrasite and Cst2 and demonstrate an H_2O-NaCl-LiCl compositions with ~6 wt.% NaCl and ~10 wt.% LiCl, and a $T_{h,tot}$ of ~300°C. L2b subtype inclusions occur in quartz and demonstrate H_2O-NaCl-LiCl-CO_2-N_2 compositions with ~12 wt.% NaCl and ~1 wt.% LiCl, and a $T_{h,tot}$ of 290°C. L2b inclusions form a liquid CO_2 phase upon cooling. Although, L2a and L2b subtype inclusions occur in cogenetic montebrasite-apatite-quartz-cassiterite assemblages, the fluid composition is dissimilar between montebrasite-Cst2 (L2a subtype) and quartz (L2b subtype). Based on the (1) the lowering in LiCl content from L2a to L2b, (2) the increase in NaCl and CO_2 content from L2a to L2b, in combination with (3) a similar $T_{h,tot}$ for both subtypes, the evolution of L2a to L2b is interpreted to be caused by montebrasite crystallization in a closed CZ. Montebrasite formation consumes Li and H_2O which, in turn, forces the pristine H_2O-NaCl-LiCl (L2a) fluid composition in the CZ towards the complementary H_2O-NaCl-LiCl-CO_2-N_2 composition (L2b). Although no measurable inclusions could be observed in the blue-colored carbonated Mn-fluoroapatite in the CZ, it is suggested that a L2b-subtype fluid was also involved in the formation of this mineral phase.

Type L3 inclusions are hosted as intergranular trails and massive 3D assemblages by mineral phases in the greisen RZ. L3 inclusions contain dominantly Na as cation. A major difference between the subtypes is the presence of a liquid CO_2 phase upon cooling in L3a inclusions. L3a subtype inclusions are hosted in quartz and show an H_2O-NaCl-(LiCl,KCl)-CO_2-(N_2) composition with ~15 wt.% NaCl and a $T_{h,tot}$ of ~280°C. L3b subtype inclusions are hosted in Cst3 and show H_2O-NaCl-(LiCl,KCl)-(CO_2,N_2) compositions with ~14 wt.% NaCl and a $T_{h,tot}$ of ~290°C. L3a and L3b inclusions are interpreted to represent the same fluid subsystem with slightly varying CO_2 partial pressures.

3 Discussion

Based on the paragenesis of the internal anatomy and the inclusions, the F-poor GDS illustrates a magmatic-hydrothermal fluid evolution from L1, L2 to L3 during solidification from the BZ inwardly to the CZ and subsolidus formation of (1) cleavelandite and (2) greisen RZs in the IZ. Inclusion petrography demonstrates the presence of magmatic saline H_2O-NaCl-KCl-(CO_2, N_2) L1 fluids during early crystallization of the WZ and IZ of the GDS. The high Na/K ratio (>> 1) of the L1 fluid is typical for a magmatic fluid which equilibrated with an evolved peraluminous melt (e.g. Audétat et al. 2000) and appears to be controlled in the GDS by microcline fractionation in the WZ and IZ. The observed decrease of the Na/K ratio in the L1 fluid is dominantly caused by

Type	Phases	System	n	Zone	Host	Size (µm)*	Fill rate (%)*	Solids	T_{fm}* (°C)	$T_{m,hh}$* (°C)	$T_{m,ice}$* (°C)	$T_{m,CO2}$* (°C)	$T_{m,clath}$* (°C)	Th_{CO2}* (°C)	$T_{h,tot}$* (°C)	N_2*(mol%)	NaCl wt.%**	LiCl wt.%**	KCl wt.%**	Salinities
L1a	S_{V1}LV	H_2O-NaCl-KCl-(CO_2-N_2)	54	WZ+IZ	Qz	10;60;23	5;32;16	paragonite, siderite, rhodocrosite, kutnohorite	-28.7;-23.4; -26.1	-22.9;-4.1; -20.3	-22.9;-15.2; -20.0	/	3.2;4.2;3.7 (n=4)	/	249;359;288	5;19;13	21.5±1.6	/	3.6±1.4	[3]
L1b	LV	H_2O-NaCl-KCl-(CO_2-N_2)	47	WZ+IZ	Qz	6;48;25	6;48;18	/	-28.1;-23.3; -25.9	-22.8;-2.3; -17.1	-22.9;-13.8; -19.4	/	-4.7;2.6;-0.9 (n=16)	/	315;389;356	3;17;12	19.7±1.8	/	2.0±1.7	[3]
L2a	(S)LV	H_2O-NaCl-LiCl	40	CZ	Mon+ Cst2	6;130;25	4;55;16	Li-mica	-79.5;-64.4; -70.1	-36.6;-28.6; -31.9	-22.5;-13.3; -17.8	/	/	/	289;304;301	/	5.54±1.3	9.84±1.1	/	[1]
L2b	(S)L_2V	H_2O-NaCl-LiCl-CO_2-N_2	27	CZ	Qz	12;54;22	17;27;22	Li-mica	-60.4;-56.0; -59.4	-22.9;-20.7; -22.2	-19.7;-15.3; -17.6	-58.1;-56.6; -57.6	2.2;3.7;2.7	16.2;20.0; 18.8 (to V)	282;304;292	5;14;7	12.3±0.3	1.0±0.5	/	[1] [2]
L3a	L_{V1}V	H_2O-NaCl-(LiCl,KCl)-CO_2-N_2	28	RZ greisen	Qz	9;31;15	12;15;13	/	-37.7;-29.8; -32.6	/	-20.1;-15.4; -17.7	-57.8;-56.6; -57.0	0.2;0.6;0.4	12.6;14.1; 13.5 (to V)	257;305;283	12;22;18	15.17±0.13	/	<0.02	[2] [3]
L3b	LV	H_2O-NaCl-(KCl)-(CO_2-N_2)	21	RZ greisen	Cst3	11;50;24	8;15;10	/	-24.3;-19.5; -21.9	/	-11.1;-9.8; -10.3		-4.7;-2.1;-3.2 (n=6)	/	254;349;289	8;25;11	14.29±0.36	/	<0.02	[3]

Values correspond to: *minimum; maximum; average **average ± standard deviation
[1] Dubois et al. (2010); [2] Bakker (1997); [3] Bodnar et al. (1989)
Cst: cassiterite; Mon: montebrasite; Qz: quartz L: liquid; S: solid; V: vapor

Table 1. Microthermometric results of the GDS.

excessive albitization. With further internal differentiation and solidification, the GDS melt-fluid system evolves to a Li-rich composition in the CZ as demonstrated by the L2 fluid. In the case of cassiterite mineralizations, literature melt-solubility data indicates that saturation of magmatic cassiterite is unlikely even for Sn-rich, highly-fractionated peraluminous systems (Štemprok 1990) like the GDS. This explains the rare occurrence of magmatic cassiterite (Cst1) in the IZ. High contents of the fluxes P and Li in the CZ cause extended fractionation by lowering the crystallization temperature which, in turn, enables Sn-saturation and the precipitation of a more significant magmatic-hydrothermal cassiterite phase (Cst2). The L3 fluid is involved in greisen formation reactions and secondary cassiterite (Cst3) precipitation.

Acknowledgements

We thank Dr. K. Piessens and Dr. S. Decrée for the access to the Raman microscope at the Royal Belgian Institute of Natural Sciences. Research of NH is funded by a postdoctoral fellowship of the Research Foundation – Flanders (FWO). The financial support by research grant C14/17/056 of the KU Leuven Research Fund is acknowledged.

References

Audétat A, Günther D, Heinrich CA (2000) Magmatic-hydrothermal evolution in a fractionating granite: A microchemical study of the Sn-W-F-mineralized Mole Granite (Australia). Geochim Cosmochim Acta 64:3373-3393.

Bakker RJ (1997) Clathrates: Computer programs to calculate fluid inclusion V-X properties using clathrate melting temperatures. Comput & Geosci 23:1-18.

Bodnar RJ, Sterner SM, Hall DL (1989) SALTY: a FORTRAN program to calculate compositions of fluid inclusions in the system NaCl-KCl-H2O. Comput & Geosci 15:19-41.

Dubois M, et al. (2010) Investigation of the H2O-NaCl-LiCl System: A Synthetic Fluid Inclusion Study and Thermodynamic Modeling from-50 degrees to+100 degrees C and up to 12 mol/kg. Econ Geol 105:329-338.

Hughes JM, et al. (2004) Mn-rich fluorapatite from Austria: Crystal structure, chemical analysis, and spectroscopic investigations. Am Mineral 89:629-632.

Jahns RH, Burnham CW (1969) Experimental studies of pegmatite genesis; I, A model for the derivation and crystallization of granitic pegmatites. Econ Geol 64:843-864.

London D, Vi GBM, Wolf MB (2001) Amblygonite-montebrasite solid solutions as monitors of fluorine in evolved granitic and pegmatitic melts. Am Mineral 86:225-233.

London D (2014) A petrologic assessment of internal zonation in granitic pegmatites. Lithos 184–187:74-104.

Maneta V, Anderson AJ (2018) Monitoring the crystallization of water-saturated granitic melts in real time using the hydrothermal diamond anvil cell. Contrib Mineral Petrol 173:83.

Penel G, et al. (1997) Infrared and Raman microspectrometry study of fluor-fluor-hydroxy and hydroxy-apatite powders. J Mater Sci Mater Med 8:271-276.

Rondeau B, et al. (2006) A Raman investigation of the amblygonite-montebrasite series. Can Mineral 44:1109-1117.

Štemprok M (1990) Solubility of tin, tungsten and molybdenum oxides in felsic magmas. Miner Depos 25:205-212.

Tacker RC (2008) Carbonate in igneous and metamorphic fluorapatite: Two type A and two type B substitutions. Am Mineral 93:168-176.

Wang R, Wu J, Dubessy J, Monchoux P (1993) Raman spectroscopy of Nb, Ta-Rich cassiterite in Beauvoir and Montebras granites, France. Chin J Geochem 12:353-390.

Webster JD, Thomas R, Rhede D, Forster HJ, Seltmann R (1997) Melt inclusions in quartz from an evolved peraluminous pegmatite: Geochemical evidence for strong tin enrichment in fluorine-rich and phosphorus-rich residual liquids Geochim Cosmochim Acta 61:2589-2604.

Assessment of scandium deportment and recovery potential in Li-Sn-W greisen deposit Cínovec/Zinnwald using EPMA, LA-ICP-MS and TIMA automated mineralogy.

Jakub Výravský[1,2] Sebastian Hreus[2], Jan Cempírek[2], Michaela Vašinová Galiová[3,4]
[1]TESCAN Brno, Czech Republic
[2]Department of Geological Sciences, Faculty of Science, Masaryk University, Czech Republic
[3]Institute of Chemistry and Technology of Environmental Protection, Faculty of Chemistry, Brno University of Technology, Czech Republic
[4]Central European Institute of Technology, Brno University of Technology, Czech Republic

Abstract. We investigated Sc content in minerals from Cínovec/Zinnwald greisen deposit. The highest content of Sc was found in ixiolite (avg. 2.09 wt.% Sc_2O_3), columbite (avg 1.34 wt% Sc_2O_3) and zircon (avg. 0.59 wt% Sc_2O_3). Three chemically distinct types of wolframite containing in avg. 0.06, 0.2 and 0.58 wt% Sc_2O_3, respectively were recognized. Cassiterite contains in average 0.068 wt% Sc. From the rock forming minerals, significant content of Sc was found only in zinnwaldite (avg. 63 ppm Sc) and muscovite (avg. 25 ppm Sc), whereas quartz, topaz, albite and K-feldspar contain very low Sc. TIMA was used to measure mineral mass proportions, grain size, deportment of elements and bulk composition of the samples. Because of low content of zircon and columbite in the studied rocks, they host significant fraction of whole rock Sc budget only in mica poor granites (~ 6 ppm Sc bulk). Higher bulk Sc concentrations in greisens are controlled predominantly by amount of micas (especially zinnwaldite) and the most Sc-rich samples (up to ~290 ppm Sc) are the ones most rich in wolframite. Grain size measurements showed, that median grain size of zircon, columbite, xenotime and ixiolite (10-40 μm) is several times lower compared to wolframite and cassiterite.

1 Introduction

Scandium is a light transitional metal with interesting applications for modern industry. The most important use of Scandium is alloying metal to Al-alloys. Al alloys with tenths of wt. % of added Sc have superior hardness and weldability (Ahmad 2003), and are used especially in the aerospace industry, resulting in lighter airplanes consuming less fuel. Other important applications are solid oxide fuel cells, where the electricity is produced directly by oxidation of the fuel (carbohydrates or hydrogen) in presence of solid electrolyte (typically Y_2O_3 doped ZrO_2). Replacement of Y_2O_3 doping with Sc_2O_3 increases ionic conductivity of the electrolyte and decreases necessary operating temperature, and therefore positively affects efficiency and lifespan of the cell (Fergus et al. 2016). Despite clear advantages of scandium, it is only seldom used, due to high prices and lack of reliable supply, so the whole market is limited to ca 10-15 t/year (USGS 2018).

Scandium abundance in the Earth's continental crust is 25 ppm in the upper and 7 ppm in the lower, respectively (Wedepohl 1995). Due to similarity in ionic radii with Fe, Mg, Mn, Al, Zr, Sn and Ti (Shannon 1976), it is usually dispersed in mafic rock-forming silicates (amphiboles, pyroxenes, Fe-Mg micas) and/or resides in some accessory minerals (garnet, tourmaline, epidote, zircon, columbite, wolframite, cassiterite, rutile, etc.). For that reason, Sc-dominant minerals and economic-grade concentrations are generally rare.

2 The Cínovec/Zinnwald deposit

The Cínovec/Zinnwald deposit is located in the Krušné hory/Erzgebirge area on border between Czech Republic and Germany (majority of the reserves lies in the Czech Republic). Geologically, it belongs to the Saxothuringian zone of the Bohemian massif of Variscan age. The deposit is bound to ca. 1.4 x 0.3 km large, N-S elongated cupola of Cínovec granite, which intruded into rhyolite-filled Teplice caldera. The granite is post-collisional, A-type, slightly peraluminous, strongly fractionated, F, Li, Rb, Sn, W, Nb and Ta-enriched intrusion (Breiter and Škoda 2012; Breiter et al 2017a). The Li-Sn-W greisen mineralization is most extensively developed in the upper part of the cupola, typically not deeper than ca 200 m below the granite-rhyolite contact surface (Breiter et al. 2017a). Four textural types of the ore bodies were recognized in the deposit (Nessler and Seifert 2015; Breiter et al. 2017a): 1) Coarse-grained, flat, up to ca 1 m thick, quartz-zinnwaldite veins with wolframite and cassiterite, which formed in fractures parallel to the granite/rhyolite contact. 2) Mineralogically and texturally similar veins with steep dip and local enrichment by base metals sulphides. 3) Relatively finer-grained greisens in massive bodies up to several tens of meters large, which formed by direct metasomatic greisenization of the original granites. 4) Flat bodies of "mineralized granites" with dispersed fine-grained cassiterite occurring in the southern part of the deposit (deeper then greisens).

Interesting contents of Sc in some ore minerals, especially wolframite, from the Cínovec/Zinnwald deposit have been known for decades, and several tens of kg of Sc-oxide were recovered from the wolframite concentrate in the 1950 s (Brožek et al. 2011). More recently, Sc content of ore minerals from various greisen deposits (including Cínovec/Zinnwald) was investigated by Kempe and Wolf (2006). Johan and Johan (1994) and Breiter et

al. (2013; 2017b; 2019) also reported Sc content of various minerals from this deposit.

With current exploration by Geomet s.r.o. evaluating the possibility of reopening the deposit, new material from recent drill holes has become available. In this contribution, we studied thin sections from all rock types (granites, greisens, hydrothermal veins) by means of EPMA and LA-ICP-MS to measure Sc content in the ore and rock-forming minerals, and we used TIMA (Tescan Integrated Mineral Analyzer) to obtain mineral mass proportions, grain size distribution, deportment of Sc, bulk sample compositions, and to understand the complex polyphase textures on the micro to macro scale.

3 Materials and methods

Twenty-three samples from the 3 drill cores lying on N-S cross-section of the deposit were obtained and 100 µm thick thin section was made from each sample. The EPMA was used to measure chemistry of wolframite, cassiterite, columbite, ixiolite, rutile, scheelite, zircon, fluorite, monazite, xenotime and micas. Trace element content of micas, quartz and feldspars were investigated by LA-ICP-MS

Fifteen samples were scanned with TIMA (Tescan Integrated Mineral Analyzer). The machine is based on SEM with BSE detector and up to 4 SDD EDS detectors and uses combination of BSE intensity and EDS spectra to distinguish boundaries of individual phases (see more in Hrstka et al. 2018). The thin sections were analyzed using “dot mapping” mode (Hrstka et al 2018) with 1 µm BSE and 5 µm EDS grid. In the dot mapping mode, the BSE image is taken first, then initial segments are found, and they are covered by EDS points in selected coarser grid. After that, image segmentation is run again, this time taking into account also EDS data, to distinguish areas with similar BSE signal but different chemistry. If a segment smaller than EDS grid spacing is found during the BSE segmentation, one EDS point is placed in center of such segment, to recognize even the smallest BSE-distinct grains (typically the ore minerals). This mode provides reasonable compromise between robustness of the data and analytical time. Average composition of phases from EPMA, trace element data from LA-ICP-MS and densities from publicly available mineral databases were loaded into TIMA software to calculate deportment of elements, mass proportion of phases and bulk sample compositions (here only Sc is discussed).

4 Results

4.1 Scandium content in ore, accessory and rock-forming minerals

From the studied minerals, the highest Sc content was found in (apparently) secondary Nb-W-Fe-rich ixiolite spatially associated with Nb-Sc-rich wolframites (avg. 2.09 wt% Sc_2O_3 and maximum value of 4.86 wt% Sc_2O_3). After the ixiolites, highest concentrations of Sc reside in columbites (avg 1.34 wt% Sc_2O_3) and zircons (avg 0.59 wt% Sc_2O_3). Three distinct types of wolframite with different minor element content were recognized: 1) Wolframite with Fe/Mn ratio close to the ferberite/hubnerite boundary with avg. ca 0.2 wt% Sc_2O_3 2) Nb-enriched wolframite with Fe/Mn ratio close to the ferberite/hubnerite boundary with avg. ca 0.58 wt% Sc_2O_3 3) near-endmember hubnerite poor in trace elements containing only 0.06 wt% Sc_2O_3 in average.

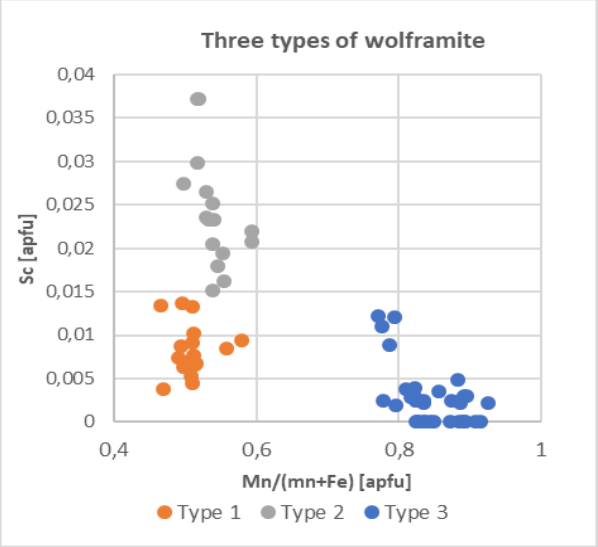

Figure 1. Plot showing 3 distinct types of wolframite, wit different Sc, Nb and Mn content. See text for explanation.

The Sc contents in Nb-Ta rich rutile and cassiterite are relatively lower, but still significant (in average 0.16 wt% and 0.068 wt% Sc_2O_3, respectively, fig. 2). From the other minerals, Sc content was discovered in xenotime (avg 0.14 wt% Sc_2O_3), however the volume proportion of xenotime is very low in all studied samples. Concentrations of Sc in fluorite and monazite were systematically below the EPMA detection limit. In scheelite replacing wolframite, only a few points showed Sc content above the detection limit.

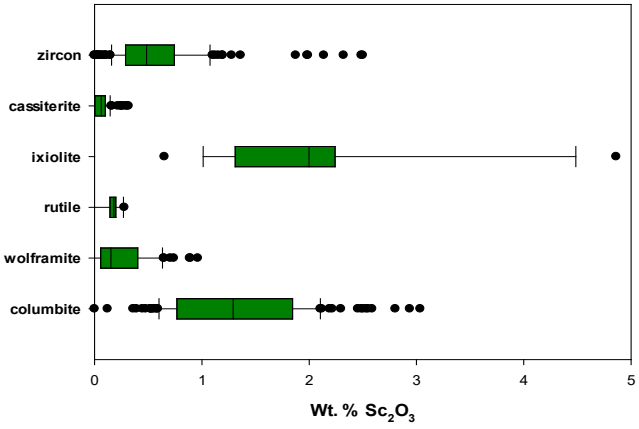

Figure 2. Box diagrams of Sc concentrations in selected minerals from Cínovec/zinnwald greisen deposit. Green boxes correspond to 2nd and 3rd quartile, vertical line in the green box represents median and the solid horizontal lines cover the range from 10 to 90% of the values.

From the rock-forming minerals investigated by LA-ICP-MS, the most important Sc-carrier by far is mica of zinnwaldite composition, containing between 43 and 88 ppm Sc, with average of 63 ppm. The zinnwaldite tends

to be more or less extensively replaced by muscovite, which could locally become the dominant mica. The Sc concentrations in secondary muscovite are about 2-3 times lower than in zinnwaldite (avg. 25.3 ppm). All other minerals are poor in scandium. Quartz contains 0.9 ppm, topaz 2.7 ppm (Breiter et al. 2013), albite < 0.5 ppm and K-feldspar 0.55 ppm.

4.2 Deportment of Sc and bulk Sc content of individual samples

Because the selected samples are very diverse with regard to rock type and content of ore minerals/micas, the differences in Sc distribution and bulk concentration will be showed on several typical examples.

1) Wolframite-rich hydrothermal vein: This sample is composed of (by mass): ~70% quartz, ~17% wolframite, ~6% micas, ~5% scheelite, ~0,12% ixiolite. Scandium is dominantly contained in wolframite (~ 87 %, 253 ppm) and ixiolite (~ 7%, 21 ppm). The total calculated Sc content of this sample is 287,7 ppm.

2) Cassiterite-rich greisen with extensive replacement of zinnwaldite to muscovite. This sample is composed of (by mass): ~60% quartz, ~21% muscovite, ~7% zinnwaldite, 1.78% cassiterite 0.02% columbite and 0.017% zircon. Scandium is dominantly contained in cassiterite (~ 41 %, 9 ppm) followed by muscovite (~ 25 %, 5.5 ppm) and zinnwaldite (~ 18 %, 4.6 ppm). Columbite and zircon host 6.8 and 4.1 % of bulk scandium, respectively. The total calculated Sc content of this sample is 22.2 ppm.

3) Mica-poor granite below the greisenized horizons. This sample is composed of (by mass): ~40% quartz, ~34% albite, ~22% orthoclase, 2.7% zinnwaldite 0.03% columbite and 0.023% zircon. Scandium is dominantly contained in columbite (~ 43 %, 2.8 ppm) followed by zinnwaldite (~ 25 %, 1.7 ppm) and zircon (~ 17 %, 1.1 ppm). The total calculated Sc content of this sample is 6.6 ppm.

4) Zinnwaldite-rich greisen with cassiterite. This sample is composed of (by mass): ~67% quartz, ~25% zinnwaldite, ~2.5% topaz, 0.54% cassiterite and 0.013% zircon. Scandium is dominantly contained in zinnwaldite (~ 75 %, 15.6 ppm) followed by cassiterite (~ 13 %, 2.7 ppm). The total calculated Sc content of this sample is 20.7 ppm.

From the obtained data it turned out, that zircon and columbite, although they are rich in Sc, are relatively significant Sc carriers only in the mica poor granites, which are generally poor in scandium (< 10 ppm bulk). The reason is their overall low abundance in the rocks (0 - 0.052 wt % for zircon and 0.002 - 0.074 wt % for columbite). The most important minerals responsible for high bulk contents of Sc in the rocks are wolframite and zinnwaldite.

4.3 Grain size distribution of relevant minerals

To understand the potential for individual Sc-bearing minerals to be recovered during ore processing, grain size distribution curves were constructed (fig.3). The grain size is expressed as ECD (Equivalent Circle Diameter – a diameter of a circle, which would have the same area as the cross-section of the grain). Because the data are too detailed, it is not possible to stitch them, therefore, grains spanning across acquisition field boundaries are actually considered as 2 or more grains, resulting in systematic bias especially for large grains (the calculated values are smaller than real). However, the primary aim of this study was to show the dramatic difference in grain size of cassiterite and wolframite compared to zircon and columbite and to assess the mass fraction of valuable minerals residing in the smallest grains, which should not be affected by this issue.

Our results (fig.3) show, that cassiterite and wolframite form much larger grains compared to zircon, xenotime, Nb-Ta rutile and columbite and that these two minerals tend to be coarser in the veins, compared to massive greisens. Zircon, xenotime, columbite and Nb-Ta rutile form significantly smaller grains with median grain size ranging generally between 10-40 µm. Although ixiolite contains the highest concentrations of Sc out of all investigated minerals, it forms typically rather small, porous, spongy-like grains, which would be probably vulnerable to extensive disintegration during crushing/milling of the ore.

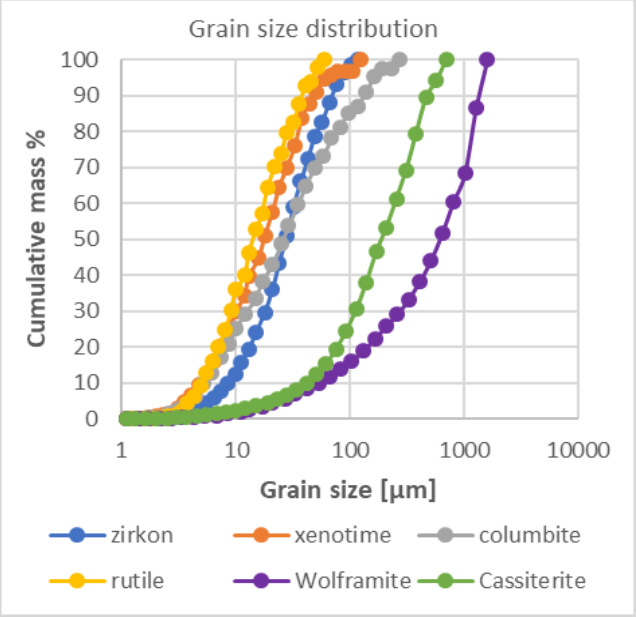

Figure 3: Cumulative grain size distribution curves for selected minerals from the Cínovec/Zinnwald deposit. The grain size is expressed as ECD (see text).

5 Conclusions

In Cínovec/Zinnwald deposit, the most important carriers of Sc in the greisens and ore veins are zinnwaldite and wolframite, whereas cassiterite becomes significant only locally in mica- and wolframite-poor samples. Granites poor in mica and ore minerals contain only about 6 ppm Sc bulk, which resides mostly in columbite and zircon. Zircon, columbite and other accessory minerals (xenotime, monazite, ixiolite…) could be potentially economically interesting due to their content of highly

prized metals (Sc, Nb, Ta, REE, Zr, Hf…), but their small grain size and low abundance complicates their recovery. On the other hand, significant concentrations of Sc (and Nb, Ta) in wolframite, zinnwaldite and cassiterite, which are the primary exploration targets could have a positive economic impact on mining operations.

The complex investigation of the samples by combination of EPMA, LA-ICP-MS and Automated mineralogy is beneficial, because on the one hand it provides (among others) quantitative data on deportment of elements in minerals, which can be used in further studies focused on understanding element behavior during magmatic, greisenization-related and post-greisenization processes, and on the other hand, we can obtain data relevant to the mining industry (grain size, associations…) at the same time from the same samples.

Acknowledgements

We thank Geomet s.r.o. for allowing us to collect the samples needed for this study.

References

Ahmad Z, 2003. The properties and application of scandium-reinforced aluminum. The Journal of The Minerals, Metals & Materials Society 55:35-39. doi:10.1007/s11837-003-0224-6

Breiter K., Škoda R (2012) Vertical zonality of fractionated granite plutons reflected in zircon chemistry: the Cínovec A-type versus the Beauvoir S-type suite. Geologica Carpathica 63(5):383-398. doi: 10.2478/v10096-012-0030-6

Breiter K, Gardenová N, Vaculovič T, Kanický V 2013. Topaz as an important host for Ge in granites and greisens. Mineralogical Magazine 77:403-417.

Breiter K, Ďurišová J, Hrstka T, Korbelová Z, Hložková Vaňková M, Vašinová Galiová M, Kanický V, Rambousek P, Knésl I, Dobeš P, Dosbaba M 2017a. Assessment of magmatic vs. metasomatic processes in rare-metal granites: a case study of the Cínovec/Zinnwald Sn–W–Li deposit, Central Europe. Lithos 292:198-217. doi: 10.1016/j.lithos.2017.08.015

Breiter K, Vaňková M, Vašinová Galiová M, Korbelová Z, Kanický V 2017b. Lithium and trace-element concentrations in trioctahedral micas from granites of different geochemical types measured via laser ablation ICP-MS. Mineralogical Magazine 81:15-33

Breiter K, Hložková M, Korbelová Z, Vašinová Galiová M 2019. Diversity of lithium mica compositions in mineralized granite-greisen system: Cínovec Li-Sn-W deposit, Erzgebirge. Ore Geology Reviews 106:12-27

Brožek V, Dušek B, Novák M 2011. Chemické listy a české skandium po 55 letech. Chemické listy 105:285-314 (in Czech).

Fergus J, Hui R, Li X, Wilkinson D.P, Zhang J, 2016. Solid Oxide Fuel Cells: Materials Properties and Performance. CRC Press, Boca Raton. 314p

Hrstka T, Gottlieb P, Skála R, Breiter K, Motl D, 2018. Automated mineralogy and petrology - applications of TESCAN Integrated Mineral Analyzer (TIMA). J. Geosci. 63:47-63

Johan, V., & Johan, Z. (1994). Accessory minerals of the Cínovec (Zinnwald) granite cupola, Czech Republic Part 1: Nb-, Ta-and Ti-bearing oxides. Mineralogy and Petrology, 51(2-4), 323-343.

Kempe U, Wolf D (2006) Anomalously high Sc contents in ore minerals from Sn–W deposits: Possible economic significance and genetic implications. Ore Geology Reviews 28:103–122.

Shannon RD (1976) Revised effective ionic radii and systematic studies of interatomic distances in halides and chalcogenides. Acta Crystallographica A32: 751–767

U.S.Geological Survey, 2018, Mineral commodity summaries 2018: U.S. Geological Survey, 200 p., https://doi.org/10.3133/70194932

Wedepohl KH (1995). The composition of the continental crust. Geochimica et Cosmochimica Acta 59:1217-1232.

Lithium, REE and trace-element contents of stanniferous-greisen mica (Rondonia Tin Province, Brazil) and their relation to REE–Sn–Rare-metal occurrence

Frederico S. Guimarães[1], Anna Luíza R. de Oliveira[1,2], Lucas Eustáquio D. Amorim[1], Francisco J. Rios[1], José Vinícius Martins[3], Renato de Moraes[3]
[1]Centro de Desenvolvimento da Tecnologia Nuclear (CDTN-CNEN)
[2]Instituto de Geociências UFMG
[3]Instituto de Geociências USP

Abstract. The Rondonia Tin Province hosts a polymetallic rare-metal association of Sn, Nb, Ta, Li, W. Mineral chemistry of Li-bearing mica from granite, greisenized granite and greisen of the province was analyzed by combined EPMA and LA-ICP-MS study. Post-magmatic micas are enriched in Li, Rb, F. Lithium incorporation in mica took place, at least partially, as coupled $Fe^{+2} + Al^{+3}$ <=> $Li^{+} + Si^{+4}$ substitution. Post-magmatic micas also show strong depletion of Sn, W, Nb, Ta and Ti. Depleted metals precipitate as oxide inclusions in the newly formed mica, such as cassiterite, rutile, ilmenite and niobates-wolframates. Heavy REE are also depleted in relation to light REE during greisenization, and HREE minerals were also found as inclusions in post-magmatic mica. Weathered siderophyllite displays the highest total-REE contents of all samples, revealing REE mobility during weathering. The observations highlight the importance of greisen micas as records of the greisenization and also as rare metal and REE reservoirs.

1 Introduction

Global REE and rare-metal (Nb, Ta, Li, W) demand is growing and strongly motivated by technological advances: their availability is critical to several high-tech industries worldwide. Granitic Sn deposits are known to bear important Nb-Ta-W-Li occurrences (Ishihara 1980; Pollard 1983; Lehmann 1990; Pirajno 2009), and evolved granites have been suggested both in Brazilian deposits and worldwide as REE hosts (Santana 2013; Santana et al. 2015; He et al. 2017).

Greisen rocks are magmatic-hydrothermal systems formed over a series of complex multi-stage metasomatic processes over highly evolved granites. During evolved granite fractional crystallization, HFSE and volatile elements are progressively enriched in fluid phases. In late- to post-magmatic periods, such fluids interact with the very granitic rock that they originated from, or its country rock, subjecting them to K-feldspathization, albitization and greisenization as the relative activities of K^{+}, Na^{+} and H^{+} change (Pollard 1983; Pollard and Taylor 1986; Pollard et al. 1987; Pirajno 2009).

Micas are the main mineral formed during greisenization (Shcherba 1970; Pollard 1983). The micas themselves tend to be Li-bearing, somewhere on the siderophyllite-zinnwaldite-polylithionite spectrum and serve as particularly good rare-metal bearers, to the point of hosting them at ratios nearly the same as the ores, and releasing them to the fluid during greisenization (Shcherba 1970). Li and trace-elements are not readily quantifiable by EPMA analyses, and while Li estimates have been used in the past, several of them exist, with varying uses and results (Tindle and Webb 1990; Tischendorf 1997, 1999).

Recent studies have developed microchemical analyses in such micas via combined EPMA and LA-ICP-MS, with reasonable success (Li et al. 2015; Xie et al. 2015; Breiter et al. 2017, 2019).

Li-bearing mica of the greisens in Rondônia Tin Province (RTP), Rondônia state, Brazil, have been previously studied in PhD theses (Leite Júnior 2002; Sparrenberger 2003), but Li and trace-element content was only available through EPMA estimates and wet chemistry, which are inconclusive. Here we provide the first combined EPMA and LA-ICP-MS analyses for Li-bearing mica for the RTP, preliminary interpretations and its implications for the REE-Sn-Rare-metal occurrences.

2 Geological Setting

The RTP is the close-second largest Sn province in Brazil. The province is in the southwest Amazonian Craton, which is a succession of SW-verging, subparallel tectono-chronological provinces, with ages spanning from the Archean to the Neoproterozoic (Cordani et al. 1979; Tassinari and Macambira 1999; Santos et al. 2008; Scandolara et al. 2013).

The RTP is hosted by the 1800 to 1550 Ma Rio Negro – Juruena Province, and consists of a series of at least seven (Bettencourt et al. 1999), possibly eight (Payolla et al. 2001; Bettencourt 2006) intrusive suites with 1606-975 Ma ages. While the latest three are the most important in respect to Sn + W + Nb + Ta ± Be mineralization, cassiterite occurrences are widespread in all suites (Isotta et al. 1978; Amorim 1999; Santos Jr. 2015; Bettencourt et al. 2016).

The studied occurrence belongs to the Younger Granites of Rondonia Suite (YGR, 995-975Ma), Santa Bárbara and Duduca batholits.

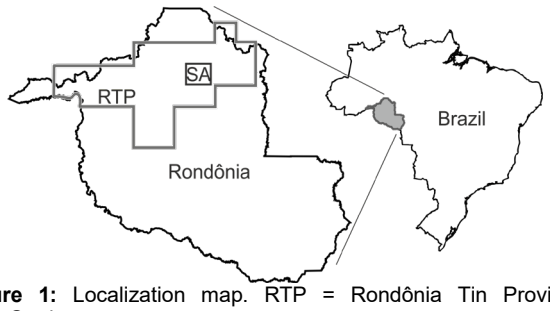

Figure 1: Localization map. RTP = Rondônia Tin Province. SA = Study area.

3 Petrography

The rocks consist of granites, greisenized granites and greisens. Granites are equi- to inequigranular and bear quartz, K-feldspar, albite and dark mica. Mica is intergranular or occurs as circular aggregates. Accessory minerals - zircon, ilmenite, rutile, fluorite, columbite, monazite, bastnäsite, britholite, topaz and cassiterite - are generally found as inclusions in mica aggregates. K-feldspathization and albitization textures are common.

Greisenized granites are equigranular rocks that preserve granitic igneous textures but had albite mostly replaced by mica. Mica hosts most accessory minerals.

Greisens are isotropic equigranular rocks that display reequilibrated textures and lack feldspar completely or almost completely. Cassiterite and columbite are abundant and occur as inclusions in dark mica.

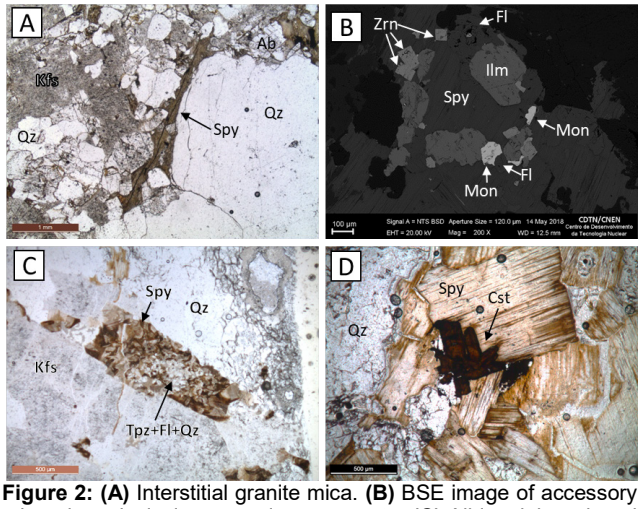

Figure 2: (A) Interstitial granite mica. **(B)** BSE image of accessory minerals as inclusions on mica aggregate. **(C)** Albite slab replaced by mica on greisenized granite. **(D)** Mica aggregate in greisen with cassiterite crystal. Cst = cassiterite; Fl = fluorite; Ilm = ilmenite; Kfs = K-feldspar; Mon = monazite; Qz = quartz; Spy = siderophyllite; Tpz = Topaz. Zrn = zircon.

4 Results

4.1 Major elements

There are two main compositional mica types in the rocks (Fig. 3A): a prevalent, trioctahedral type (siderophyllite grading to lithian siderophyllite), and a dioctahedral type (muscovite to lithian muscovite). Lithium estimates based on EPMA SiO_2 content were more or less fitting for trioctahedral micas but lacking for dioctahedral (Fig. 3B). Lithium estimates based on F content were satisfactory for all mica types (Fig. 3C). Because of that, samples without LA-ICP-MS analyses had their Li content estimated via F content.

The trioctahedral and dioctahedral types are mainly separated by their Si, Al, Fe, Ti, Li and F content, as the Li-siderophyllite series is richer in the latter four. Additionally, the trioctahedral series displays negative Fe + Al (IV) x Si + Li correlation (Fig. 3D).

MgO and Na_2O contents are very low in all mica types (<1.8% and <0.3% respectively).

4.2 REE and trace elements

The rare metals (Nb, Ta, W) plus Ti and Sn show positive correlations, particularly amongst Li-siderophyllite (Fig. 4A). Highest rare metal and Sn contents are observed in mica from granites, and a few samples of mica from greisenized granite, a trend opposite to Li (Fig. 4B). Greisen mica follows with intermediate values, and the remaining mica samples from greisenized granites display the lowest values (samples circled in Fig. 4).

Total REE (REEt) content varies from <1 ppm to ~800 ppm, and lithology has no influence in it. However, the ratio between light REE and total REE is highly dependent on lithology (Fig. 4C). Mica from granites show the lowest values of this ratio while greisens display the highest. Some mica from greisenized granites has intermediate values, while others have ratios as high as the ones from greisen. Weathered siderophyllite displays higher REE totals amongst samples (samples marked with rectangles in Fig. 4).

5 Discussion

SiO_2-based Li estimates assume Li is incorporated via the coupled substitution $Fe^{+2} + Al^{+3} <=> Li^{+} + Si^{+4}$ at the octahedral and tetrahedral site. This mechanism is present in trioctahedral mica as evidenced by the negative Fe + Al (IV) x Si + Li correlation (Fig. 3D) The correlation is present but not at a perfect 1:1 ratio, indicating another mechanism should also be in effect. Dioctahedral micas, on the other hand, show no correlation of these values (Fig. 3B) suggesting another Li-incorporation mechanism is predominant. This hypothesis also explains why SiO_2-based Li estimation was not accurate.

Lithium is a good proxy for greisenization since its contents rise consistently from granitic (magmatic) siderophyllite to greisenized-granite and greisen (postmagmatic) siderophyllite, towards the lower-left corner of the Mgli x Feal diagram (Fig. 3A). Mgli stands for Mg – Li and Feal for Fe(t) + Mn + Ti – Al (IV), in apfu (Tischendorf, 1997). Incipient weathering of siderophyllite moves samples towards the upper-right corner as Li is lost and Mg and Fe added.

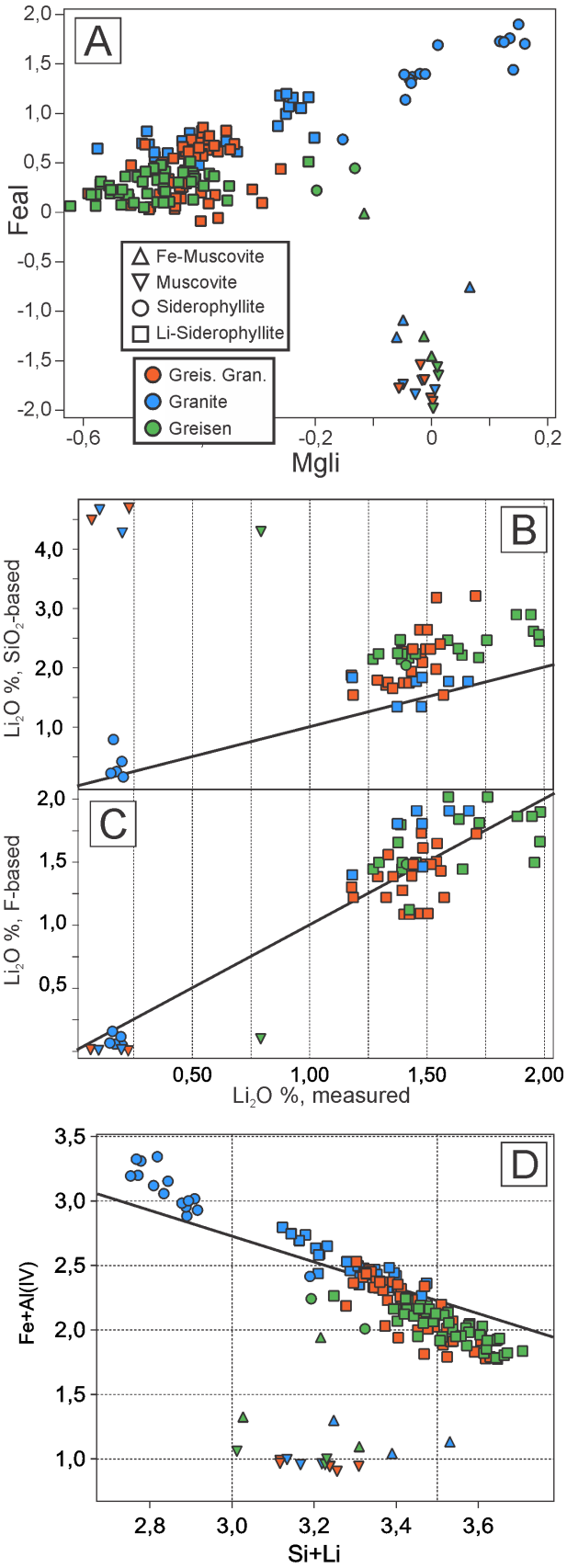

Figure 3. (A) Mgli versus Feal plot (Tischendorf, 1997). **(B-C)** Li_2O as measured via LA-ICP-MS versus Li_2O estimates based on EPMA SiO2 and F content respectively. Solid lines have a slope of 1. **(D)** Fe+Al versus Si + Li plot, apfu. Solid line has a slope of -1.

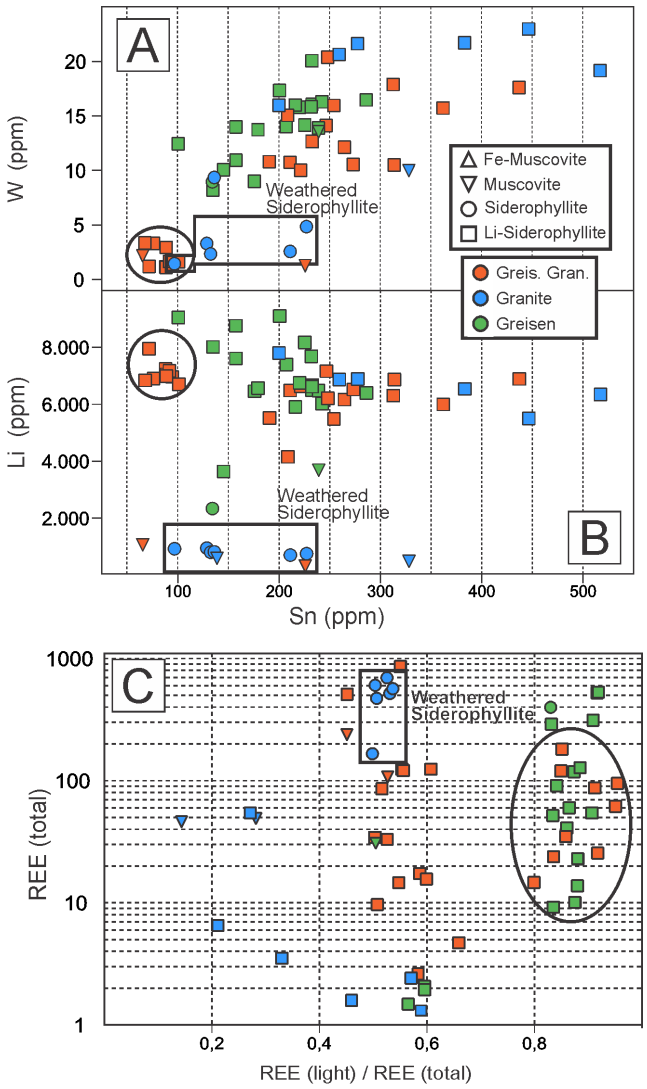

Figure 4. A-B: Sn in ppm versus W and Li respectively. **C:** Ratio of Light REE / REE(total) versus REE (total) in ppm.

Dioctahedral micas bear little to no Li and have been interpreted as a late sericitization event. Magmatic mica hosts the highest contents of rare metal and Sn, and the lower contents observed occur in post magmatic mica from greisenized granite. Greisenized granites also retain some preserved igneous mica that bears high rare-metal content. Greisen texture has been fully reequilibrated, so mica trace-element composition cannot be distinguished between magmatic and post-magmatic stages. Greisenization seems to produce mica relatively depleted in HREE and enriched in LREE when compared to magmatic mica.

6 Implications

Micas are thought to be important reservoirs of Sn and rare metals in evolved granites (Shcherba 1970). During greisenization, said elements can be partitioned to the fluid and/or to precipitate as mineral inclusions as new mica is formed (Pirajno 2009). This process seems to be instrumental to ore formation at the RTP, particularly as

greisens and greisenized granites host cassiterite, niobates and wolframates mainly as inclusions on mica.

Moreover, while LREE minerals were observed as inclusions in mica in all rock types, HREE minerals were observed only as inclusions in mica from greisen and greisenized granite. Similarly, it is suggested that relative depletion in HREE from magmatic micas during greisenization could trigger HREE mineral formation.

High REE content on weathered siderophyllite suggests weathering has some bearing on REE mobilization on evolved granites.

Acknowledgements

We thank chief exploration geologist Henrile Meireles for access and support, CNPq (Projects 424909/2016-2 and 308781/2014-7), FAPEMIG (Project PPM 00357-17) and CDTN/CNEN (project 0614.26)

References

Amorim JL (1999) Recursos Minerais. In: Scandolara J (ed) Geologia e Recursos Minerais do Estado de Rondônia. CPRM, Brasília, pp 67–76

Bettencourt JS (2006) SHRIMP-RG U-Pb ZIRCON GEOCHRONOLOGY OF GNEISS FROM THE RIO CRESPO INTRUSIVE SUITE , SW AMAZONIAN CRATON , RONDÔNIA , BRAZIL : New insights about Protolith crystallization and metamorphic ages. In: South American Symposium on Isotope Geology. pp 49–52

Bettencourt JS, Juliani C, Xavier RP, et al (2016) Metallogenetic systems associated with granitoid magmatism in the Amazonian Craton : An overview of the present level of understanding and exploration significance Journal of South American Earth Sciences Metallogenetic systems associated with granitoid m. J South Am Earth Sci 68:22–49. doi: 10.1016/j.jsames.2015.11.014

Bettencourt JS, Tosdal RM, Leite WB, Payolla BL (1999) Mesoproterozoic rapakivi granites of the Rondonia Tin Province, southwestern border of the Amazonian craton, Brazil-I. Reconnaissance U-Pb geochronology and regional implications. Precambrian Res 95:41–67. doi: 10.1016/S0301-9268(98)00126-0

Breiter K, Hložková M, Korbelová Z, Galiová MV (2019) Diversity of lithium mica compositions in mineralized granite–greisen system: Cínovec Li-Sn-W deposit, Erzgebirge. Ore Geol Rev 106:12–27. doi: 10.1016/j.oregeorev.2019.01.013

Breiter K, Vaňková M, Galiová MV, et al (2017) Lithium and trace-element concentrations in trioctahedral micas from granites of different geochemical types measured via laser ablation ICP-MS. Mineral Mag 81:15–33. doi: 10.1180/minmag.2016.080.137

Cordani UG, Tassinari CCG, Teixeira W, et al (1979) Evolução Tetônica da Amazônica com Base nos dados Geocronológicos. In: Segundo Congreso Geologico Chileno. Arica, p 12

He C, Xu C, Zhao Z, et al (2017) Petrogenesis and mineralization of REE-rich granites in Qingxi and Guanxi, Nanling region, South China. Ore Geol Rev 81:309–325. doi: 10.1016/j.oregeorev.2016.10.021

Ishihara S (1980) The granitoid Series and Mineralization. doi: 10.1590/S1516-18462008000300012

Isotta CAL, Carneiro JM, Kato HT, Barros RJL (1978) Projeto Província Estanífera de Rondônia. Porto Velho

Lehmann B (1990) Metallogeny of Tin. Springer-Verlag

Leite Júnior WB (2002) A Suíte Intrusiva Santa Clara (RO) e a Mineralização primária polimetálica (Sn, W, Nb, Ta, Zn, Cu, Pb) Associada. Universidade de São Paulo

Li J, Huang XL, He PL, et al (2015) In situ analyses of micas in the Yashan granite, South China: Constraints on magmatic and hydrothermal evolutions of W and Ta-Nb bearing granites. Ore Geol Rev 65:793–810. doi: 10.1016/j.oregeorev.2014.09.028

Payolla BL, Bettencourt JS, Leite Jr WB, Basei MAS (2001) The rio Crespo intrusive suite: Geological U-Pb and Sm-Nd isotopic evidence for a major 143 Ga arc-related magmatism in the Rondonia state, SW Amazonian craton, Brazil. In: 3 South American symposium on isotope geology Extended abstracts. Servicio Nacional de Geologia y Mineria, Chile, p 642

Pirajno F (2009) Hydrothermal processes and mineral systems

Pollard PJ (1983) Magmatic and postmagmatic processes in the formation of rocks associated with rare-elements deposits.pdf. Trans Inst Min Metall (Section B Appl Eart Sci 92:

Pollard PJ, Pichavant M, Charoy B (1987) Contrasting evolution of fluorine- and boron-rich tin systems. Miner Depos 22:315–321. doi: 10.1007/BF00204525

Pollard PJ, Taylor RG (1986) Progressive Evolution of Alteration and Tin Mineralization: Controls by Interstitial Permeability and Fracture-Related Tapping of Magmatic Fluid Reservoirs in Tin Granites. Econ Geol 81:1795–1800. doi: 10.1055/s-2002-30668

Santana IV (2013) Caracterização Mineralógica e Geoquímica de Ocorrências de Terras Raras no Maciço Granítico Serra Dourada, Goiás/Tocantins, Brasil

Santana I V, Wall F, Botelho NF (2015) Occurrence and behavior of monazite-(Ce) and xenotime-(Y) in detrital and saprolitic environments related to the Serra Dourada granite, Goiás/Tocantins State, Brazil: Potential for REE deposits. J Geochemical Explor 155:1–13. doi: 10.1016/j.gexplo.2015.03.007

Santos JOS, Rizzotto GJ, Potter PE, et al (2008) Age and autochthonous evolution of the Sunsás Orogen in West Amazon Craton based on mapping and U-Pb geochronology. Precambrian Res 165:120–152. doi: 10.1016/j.precamres.2008.06.009

Santos Jr. PSM (2015) Metalogênese do Depósito de Estanho Liberdade, Campo Novo de Rondônia - RO. Universidade de Brasília

Scandolara JE, Fuck RA, Dantas EL, Souza VS (2013) Geochemistry of Jamari complex, central-eastern Rondônia: Andean-type magmatic arc and Paleoproterozoic crustal growth of the southwestern Amazonian Craton, Brazil. J South Am Earth Sci 46:35–62. doi: 10.1016/j.jsames.2013.04.002

Shcherba GN (1970) Greisens. Int Geol Rev 12:114–150. doi: 10.1080/00206817009475216

Sparrenberger I (2003) Evolução da Mineralização Primária Estanífera Associada ao Maciço Granítico Santa Bárbara, Rondônia. Universidade de São Paulo

Tassinari CGCG, Macambira JB (1999) Geochronological provinces of the Amazonian Craton. Episodes Episodes,:174–182. doi: 10.1080/00206819709465329

Tindle AG, Webb PC (1990) Estimation of lithium contents in trioctahedral micas using microprobe data: application to micas from granitic rocks. Eur J Mineral 2:595–610. doi: 10.1127/ejm/2/5/0595

Tischendorf G (1999) The Correlation Between Lithium and Magnesium in Trioctahedral Micas: Improved Equations for Li2O Estimation from MgO Data. Mineral Mag 63:57–74. doi: 10.1180/minmag.1999.063.1.07

Tischendorf G (1997) On Li-Bearing Micas: Estimating Li from Electron Microprobe Analyses and an Improved Diagram for Graphical Representation. Mineral Mag 61:809–834. doi: 10.1180/minmag.1997.061.409.05

Xie L, Wang RC, Groat LA, et al (2015) A combined EMPA and LA-ICP-MS study of Li-bearing mica and Sn-Ti oxide minerals from the Qiguling topaz rhyolite (Qitianling District, China): The role of fluorine in origin of tin mineralization. Ore Geol Rev 65:779–792. doi: 10.1016/j.oregeorev.2014.08.013

Discovery, delineation and development of Australia's first caesium deposit: Exploration implications from applied technology.

Nigel W. Brand
Geochemical Services Pty Ltd, The University of Western Australia

David J. Crook, Stuart T. Kerr, Russel N. Panting
Pioneer Resources Limited

Sophie O. Perring. Christabel J. Brand
Portable XRF Services Pty Ltd

Abstract. The Sinclair Caesium Deposit, discovered in 2016, delineated in 2017 and developed in 2018, is Australia's first mining operation to commercially extract the caesium-rich mineral pollucite. Economic caesium deposits are extremely rare, with only three known mining operations having produced commercial quantities of pollucite, including the Bernic Lake Mine (Manitoba, Canada), Bikita Mine (Zimbabwe) and the Sinclair Mine (Western Australia).

The formation of pollucite only occurs in extremely differentiated complex lithium-caesium-tantalum (LCT) pegmatites and given their size and rarity, caesium-rich deposits globally are either challenging to explore for or failed to form during the emplacement of the LCT pegmatite. The discovery and development of the Sinclair Caesium Mine has provided a rare opportunity to examine an extremely differentiated complex LCT pegmatite with applied technologies to provide an insight for future discoveries of economic caesium deposits.

1 Introduction

The announcement of a significant caesium (Cs) intersection (6m at 25.7% Cs_2O) associated with lithium-caesium-tantalum (LCT) pegmatites on the Pioneer Dome was reported by Pioneer Resources Ltd (PIO) on 4th October 2016 (PIO ASX 2016a). Follow-up drilling delineated a cluster of pollucite lenses, named the Sinclair Caesium Deposit (Sinclair), with an initial Mineral Resource Estimate of "10 500 t of the caesium ore pollucite with a grade of 17.1% Cs_2O" (PIO ASX 2017). The commencement of mining operations was reported on 13th September 2018 (PIO ASX 2018), less than 2 years from discovery.

Pollucite $[(Cs,Na)_2(Al_2Si_4O_{12})\ 2H_2O]$ is a rare mineral with a high value attributed to its high caesium content (~29.66% Cs2O) which forms in extremely differentiated LCT pegmatite systems. Global supply is very constrained, and world resource estimations are unavailable (USGS, 2019). Caesium metal is sold in limited quantities under confidential contracts so a true market price is unavailable.

The uses of Cs include: the production of photoelectric cells, energy conversion devices such as fuel cells, magneto-hydrodynamic generators and polymer solar cells, however its main use is in the manufacture of caesium formate brine, a heavy liquid (1.8 to 2.4 g/cm^3) used in high-pressure, high-temperature well drilling for oil and gas.

2 Location and geological Setting

The Sinclair Caesium Deposit is located 35 km north-north west of Norseman in Western Australia or 125 km south-south east of Kalgoorlie.

The mine is located within the Archaean-aged Yilgarn Craton of Western Australia, within the Coolgardie Domain of the Norseman –Wiluna Greenstone Belt. The Coolgardie Domain is dominated by two large granitoid domes, the Pioneer and Widgiemooltha Domes; the long axes of which trend north to north-northwest respectively. The younger Binneringie Dyke, an east-west trending Proterozoic dyke, transects the sequence between the Widgiemooltha and Pioneer Domes.

The Pioneer Dome is defined by a granitoid core which has intruded older Archaean-aged gneiss (Fifty Mile Tank Gneiss) and a greenstone sequence. The greenstone sequence comprises a mafic suite (black shale, ultramafic and mafic volcanics, and gabbro intrusions) which in turn has been stratigraphically overlain by a thick sedimentary sequence. Pegmatite bodies have preferentially intruded into the greenstone sequence. The Pioneer Dome and surrounding lithoscape has been metamorphosed to greenschist and lower-amphibolite facies and has been multiply deformed resulting in isoclinal folding (Griffin 1989).

At least 13 clusters of pegmatites, including LCT pegmatites, have been identified along a 20 km strike length on the eastern flank of the Pioneer Dome (Fig 1). The East Pioneer pegmatite corridor comprises a narrow (<1 km wide) mafic suite of rocks trending roughly north-south, faulted up against the Fifty Mile Tank Gneiss. This corridor is dominated by strong north-south cleavages and pegmatite dykes occur in both the gneiss and greenstones (Griffin 1990). To date the only available dating is of the Fifty Mile Tank Gneiss dated at ≥ 2664 ± 5 Ma (Nelson 1997).

The pegmatite wall zones typically consist of quartz, K and Na feldspars, and muscovite, while core zone minerals include biotite, lepidolite, petalite, pollucite

(where present), tourmaline, and beryl.

Less deformed pegmatites consistently cut more deformed pegmatites which suggest that there were several episodes of pegmatite intrusion.

3 Discovery and applied technology

Conventional soil samples were collected over mapped pegmatites within the mafic-ultramafic stratigraphy of the East Pioneer pegmatite corridor. All soil samples were analysed using a lithium-Index Calibration developed for a field portable XRF in association with Pioneer as a proxy for lithium (PIO 2016a); used to prioritise areas of interest in the field.

Confirmation four-acid ICP-MS laboratory analyses were undertaken prior to detailed prospect mapping, rock chip sampling and a decision to drilling. Over 7,000 soil samples identified nine high priority and 15 mid-rank targets including PEG008a, host to the Sinclair.

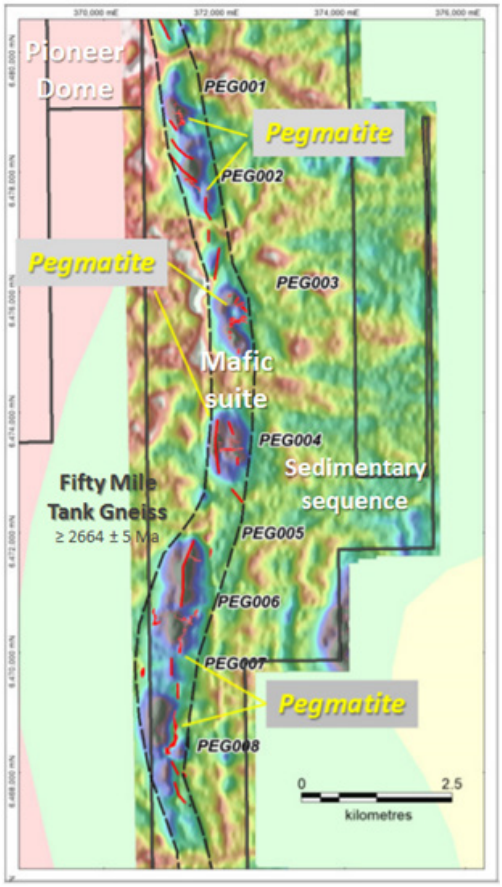

Figure 1. East Pioneer pegmatite corridor showing outcropping pegmatites (red) and main geological units in relation to total count (U, Th, K) radiometric image (PIO 2016b).

Commencement of an inaugural 5000m RC drilling programme in mid-2016 (PIO 2016b) identified both high grade lithium and caesium (PIO 2016a) being the discovery hole for the Sinclair Zone Caesium Deposit.

The discovery of pollucite and its subsequent extraction through mining provided Pioneer with a unique opportunity to investigate and understand the geology, mineralogy and geochemistry of such a rare deposit style and provide insights for future exploration of caesium-rich deposits.

During the delineation and development of the Sinclair Mine, in addition to conventional laboratory four acid, fusion XRF assays and XRD mineral identification, a range of new, or more readily available, technologies were employed. These included RAMAN spectroscopy, short-wavelength infrared spectroscopy (SWIR), fourier-transform infrared spectroscopy (FT-IR), portable XRF (pXRF) and micro-XRF (μXRF).

Throughout the extraction of the pollucite mineralisation pXRF was exclusively used for grade control, enabling rapid and accurate dataflow. RAMAN spectra for mineral identification were collected from grade control samples and are being used to augment geological mapping and mineral zonation definition ahead of the Company embarking on further exploratory drilling.

4 Sinclair LCT pegmatite

4.1 Pegmatite lithogeochemistry

Benchmarked against other known LCT pegmatites, the host pegmatite of Sinclair shows a very distinct and unique chemistry reflecting its extreme fractionation (Fig 2). The geochemistry of Sinclair will be discussed further in the talk.

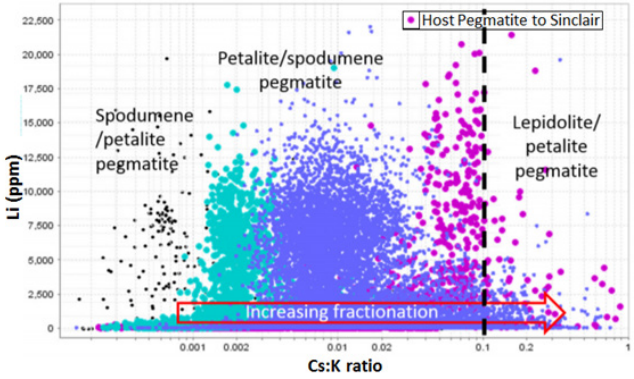

Figure 2. Cs:K ratio vs Li from three LCT pegmatites showing the extreme fractionation undertaken at Sinclair (purple).

4.2 Geology and mineralogy

Common with the Bernic Lake and Bikita Deposits, the Sinclair Deposit host LCT pegmatite consists of an outer pegmatite wall zone that is coarse grained, and dominated by plagioclase feldspar, muscovite and quartz with accessory garnet, tourmaline and beryl and an inner core zone composed of, in decreasing order, quartz, albite (cleavelandite), lepidolite, pollucite, petalite, zinnwaldite, eucryptite, beryl, amblygonite and topaz. The core zone is 'capped' by a thick (~35-40m) monomineralic potassium feldspar zone (Fig 3).

The pollucite mineralisation is monomineralic, similar to the Bernic Lake Deposit (London 2018), and forms small (~2-10m) discreet pods spatially associated with albite (cleavelandite), lepidolite, petalite and quartz.

To date, very minor instances of spodumene have

been detected, unlike pollucite zones described from Tanco (Stilling et al 2006) and Bikita (Dittrich et al 2018).

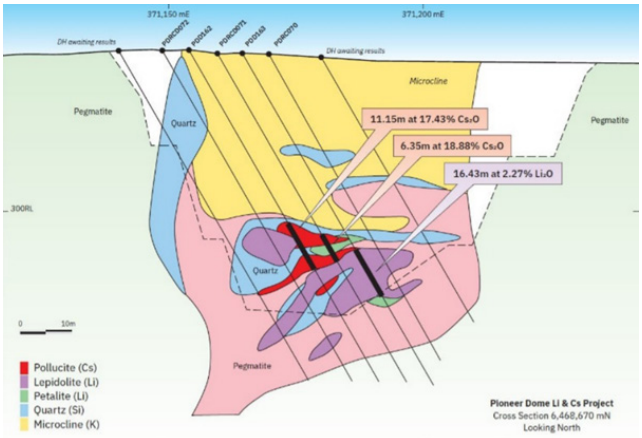

Figure 3. Geological cross section of Sinclair at 6468670mN with diagrammatic pit outline.

4.3 Mineral and chemical zonation in the core zone

During the development of the Sinclair Mine, grade control sampling was analysed using a matrix match Cs calibration on a countertop CTX XRF instrument, enabling rapid assay turnaround, which was of paramount importance due to the short time scale of operational cycles of the mining operation.

The use of the CTX pRFX instrument provided a comprehensive geochemical dataset, albeit without a Li analysis at the time.

To verify the presence of and distinguish between white lithium silicate minerals (eg petalite, eucryptite and spodumene) a RAMAN spectrometry application was developed.

Integrated results from the pXRF and RAMAN spectroscopy show a central core of discrete pollucite pods associated with quartz flanks and zoned by lepidolite and albite (cleavelandite). Zinnwaldite, petalite and eucryptite occur further outboard (Fig 4).

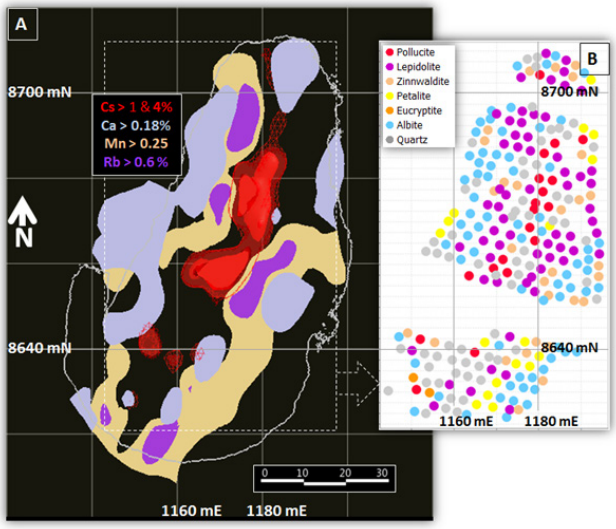

Figure 4. Plan section of Sinclair at 295 m RL showing a) selected element concentration analyzed by pXRF and b) dominant mineral phase identified by RAMAN spectroscopy. Both data sets showing element and mineral zonation associated with the pollucite in the central core zone.

4.4 Pegmatite weathering

Published data on pegmatite weathering, associated regolith development and landscape evolution is rare to non-existent; and is a knowledge gap when exploring for LCT Pegmatites in deeply weathered terrains such as the Yilgarn Craton.

During the development of the Sinclair Deposit, zones of weathered pollucite were encountered typically associated with contacts and structures along which groundwater had penetrated. Weathered material collected during mining is being investigated using µXRF following a successful trial which showed invading Ca and Sr veinlets from groundwater penetrating into amblygonite (Fig 5).

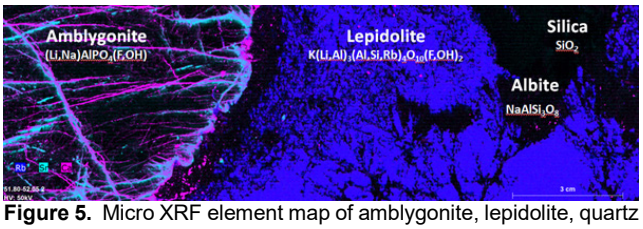

Figure 5. Micro XRF element map of amblygonite, lepidolite, quartz and albite (cleavelandite) from PDD167; 51.80 to 52.05 mdh showing invading Ca and Sr veinlets in amblygonite from penetrating ground waters.

5 Discussion and exploration implication

The discovery of a rare caesium deposit and its host LCT pegmatite has provided an opportunity to investigate and thus improve understanding of this style of mineralization utilizing Pioneer's extensive exploration and mining data sets to develop models for future discoveries.

The ongoing research into the geological setting of Sinclair has demonstrated its unique lithogeochemical signature and mineralogical characteristics of both fresh and weathered samples, using applied technologies that provide tools and applications that will be utilised in future exploration for Cs-rich LCT pegmatites.

Acknowledgement

The authors wish to acknowledge the effort of Pioneer Resources Limited staff, consultants and contractors associated with the discovery, delineation and development of Sinclair, Australia's first caesium mine and the continued and ongoing support from the Pioneer's Board of Directors.

References

Dittrich T, Seifert T, Schulz B, Hagemann S, Gerdes A, Pfänder J (2018) Lithium-Cesium-Tantalum pegmatites in Zimbabwe and Western Australia, and the formation of Neo-Archean massive (Cs)-pollucite mineralisations 10.13140/RG.2.2.14118.98888.

Griffin TJ (1989) Widgiemooltha, Western Australia. Geological Survey of Western Australia 1:250,000 Geological Series

Explanatory Notes.
Griffin TJ (1990) Geology of the Granite-Greenstone Terrane of the Lake Lefroy and Cowan 1:100 000 sheets, Western Australia: Western Australia Geological Survey, Report 32, 53p.
London D (2018) Ore-forming processes within granitic pegmatites. Ore Geol Rev 101:349-383.
Nelson DR (1997) Evolution of the Archaean granite-greenstone terranes of the Eastern Goldfields, Western Australia: SHRIMP U-Pb zircon constraints. Precam Res 83: 57-81.
Pioneer Resource Limited (2016a) Lithium-caesium discovery at Pioneer Dome. http://www.pioneerresources.com.au/downloads/asx/pio20161 00401.pdf
Pioneer Resource Limited (2016b) Pioneer announces a 5,000m RC drilling programme at its Pioneer Dome lithium project. http://www.pioneerresources.com.au/downloads/asx/pio20160 72701.pdf
Pioneer Resource Limited (2017) Mineral resource estimate for the Sinclair Caesium Project. http://www.pioneerresources.com.au/downloads/asx/pio20170 32201.pdf
Pioneer Resource Limited (2018) Pioneer commences mining operations at Sinclair caesium mine. http://www.pioneerresources.com.au/downloads/asx/pio20180 91301.pdf
Stilling A, Černý P Vanstone PJ (2006) The Tanco pegmatite at Bernic Lake, Manitoba.
Xvi. Zonal And Bulk Compositions And Their Petrogenetic Significance. Can Min 44:599-623.
U.S. Geological Survey (2018) Mineral commodity summaries 2018: USGS 200 p https://doi.org/10.3133/70194932.